Registration of 3D Intraoperative MR Images of the Brain Using a Finite Element Biomechanical Model

Matthieu Ferrant[1,2,*], *student Member, IEEE*, Arya Nabavi[2,3], Benoît Macq[1], *Senior Member, IEEE*, Ferenc A. Jolesz[2], Ron Kikinis[2], and Simon K. Warfield[2], *Member, IEEE*

Abstract— **We present a new algorithm for the non-rigid registration of 3D Magnetic Resonance (MR) intraoperative image sequences showing brain shift. The algorithm tracks key surfaces of objects (cortical surface and the lateral ventricles) in the image sequence using a deformable surface matching algorithm. The volumetric deformation field of the objects is then inferred from the displacements at the boundary surfaces using a linear elastic biomechanical finite element model. Two experiments on synthetic image sequences are presented, as well as an initial experiment on intra-operative MR images showing brain shift. The results of the registration algorithm show a good correlation of the internal brain structures after deformation, and a good capability of measuring surface as well as subsurface shift. We measured distances between landmarks in the deformed initial image and the corresponding landmarks in the target scan. Cortical surface shifts of up to 10mm and subsurface shifts of up to 6mm were recovered with an accuracy of 1mm or less and 3mm or less respectively.**

Keywords—**Intraoperative image registration, brain modeling, finite element method, tetrahedral mesh generation.**

I. Introduction

A. Image-Guided Neurosurgery

The development of image guided surgery systems has fostered significant improvements in minimally invasive surgery over the last decade. Such systems have been increasingly used in neurosurgery and have been shown to improve surgical visualization and navigation, and to reduce the amount tumor remaining after surgery [30], [32].

However, image-guided neurosurgery (IGNS) has brought to prominence the problem of brain shift, the shape deformations the brain undergoes during surgery. The main factors causing this deformation include the loss of cerebrospinal fluid (CSF), the injection of anaesthetic agents, and the actions of the neurosurgeon (such as resection and retraction). These deformations can significantly diminish the accuracy of neuronavigation systems ([6], [35], [43]), and it is therefore of great importance to be able to quantify and correct for these deformations by updating pre-operative imaging during surgery.

B. Non-Rigid Registration for IGNS

Previous work that has been done for capturing non-rigid intraoperative volumetric deformations can be categorized by those using image-based models and those using biomechanical models. Image-based models are often used when intraoperative image acquisition is available.

B.1 Image-based models

Image-based models propose to locally satisfy an image similarity criterion under a given regularization constraint. The main assumption of such methods is constant intensity and small displacements between the images to be matched. If such algorithms are run in multiresolution and if noise and intensity variation artifacts can be corrected for, good results can be obtained from a purely visual point of view (recent examples include [28], [13], [26], [29], [27]). However, such methods tend to only establish correspondences between local image structures and arbitrarily interpolate between these, without accounting for prior knowledge one has about the imaged objects (such as inhomogeneity and anisotropy).

To cope with this issue, physical deformation models have been proposed to constrain a deformation field computed from image data using elastic (e.g. [5], [1], [20], [56], [11], [16]) and viscous fluid deformation models (e.g. [7], [4]). However, in these works the physical models were just used as a better regularization constraint on the image similarity criterion, without incorporating specific material properties (such as hard/soft parts, etc.).

It is only recently that biomechanical models have been explicitly proposed to constrain the registration of images (e.g. [33], [50], [25]) in the context of deformable brain registration. Peckar et al. [50] describe a framework for registering 3D images given prescribed correspondences and an elastic deformation model to infer a volumetric deformation field. Even though the algorithm was applied on 3D synthetic data, it was only tested in 2D on medical images. Following this work, Hagemann et al. [25], [24] developed a 2D biomechanical model of the head to register brain images showing deformations due to neurosurgical operations. The model is deformed by enforcing correspondences between landmark contours manually or semi-automatically. The constitutive equations of the biomechanical model are discretized using finite elements (FE), and the basic elements of the mesh are the pixels of the image, which causes the computations to be particularly heavy.

Kyriacou et al. [33] study the effect of tumor growth in brain images for doing atlas registration. They use a FE model and apply concentric residual strain to the tumor boundary to shrink it before the actual atlas registration.

Currently, the drawback of such methods is that they either require user intervention, or another not fully automated means to

* Corresponding Author. MF is now with General Electric Medical Systems, Buc, France.
[1] Communications and Remote Sensing Laboratory, Université catholique de Louvain, B-1348 Louvain-la-Neuve, Belgium. E-Mail: {ferrant,macq}@tele.ucl.ac.be
[2] Surgical Planning Laboratory, Department of Radiology, Brigham and Women's Hospital and Harvard Medical School, Boston MA 02115, USA. E-Mail: {arya,jolesz,kikinis,warfield}@bwh.harvard.edu
[3] Department of Neurosurgery, University of Kiel, Germany.

compute the forces (or correspondences) applied to the model. Another drawback is that these methods have only been applied to 2D medical images thereby limiting the clinical utility and the possibility to efficiently assess the accuracy of the method.

The cardiac image analysis community has also been using physics-based models - mainly FE models - they deform with image-derived forces. These models then provide quantitative, and physically interpretable 3D deformation estimates from image data. Papademetris et al. [46] derive the forces they apply to the FE model from Ultrasound (US) images using deformable contours they match from one image to the next one using a shape-tracking algorithm. Metaxas et al. [36] derive their forces from MRI-SPAMM data for doing motion analysis of the left or right ventricle [47], [23]. These approaches are very interesting and a generic parameterized FE model is usually fit onto the image sequence before doing the analysis.

B.2 Simulation models

In the context of brain shift analysis, there has been a significant amount of work directed towards simulation using models driven by physics-based forces such as gravity. Skrinjar et al. [51], [53] have proposed a model consisting of mass nodes interconnected by Kelvin models to simulate the behavior of brain tissue under gravity, with boundary conditions to model the interaction of the brain with the skull. They recently presented a new implementation of their system [52] using a linear elasticity model driven by surface correspondences they extract from intraoperative MR images with the goal of eventually being able to extract these surface correspondences from intraoperative stereo cameras.

Miga et al. [49], [39], [38], [40] proposed a Finite Element (FE) model based on consolidation theory where the brain is modeled as an elastic body with an intersticial fluid. They also use gravitational forces, as well as experimentally determined boundary conditions. A limiting factor of their implementation is that the preoperative segmentation and mesh generation require about five hours of operator time.

Miller et al. [41], [42] carried out exceptional modeling work and presented simulations and comparisons with in-vivo experiments demonstrating that a hyper-viscoelastic constitutive model can accurately reproduce brain deformation for compression levels reaching 30% and for loading velocities varying over five orders of magnitude.

Even though these simulation models are very promising, it remains difficult to accurately estimate all the forces and boundary conditions that interact with the model during neurosurgery. For instance, it is very difficult to model the shrinking of the lateral ventricles during brain shift. This phenomenon is probably due to a pressure change of the cerebro-spinal fluid (CSF) inside the ventricles [43], but it is extremely complicated to effectively measure this pressure continuously during neurosurgery. The clinical application of simulation models will be very extremely useful when it will be possible to intraoperatively measure the localization and associated forces of surgical instruments (such as the retractor, etc.).

C. *Proposed Method*

Our ultimate goal is to be able to update preoperative images during surgery for improving intraoperative navigation and tumor resection, and of reducing the amount of intraoperative imaging that is necessary. To be able to do this, one first needs to validate a non-rigid deformation model. Intraoperative MR imaging provides reasonable contrast and spatial resolution, which makes it an ideal testbed for developing and validating nonrigid deformation methods.

In our deformable registration method, we propose to merge the prior biomechanical knowledge physicians have about the internal structure of the object that is being imaged (e.g. inhomogeneities, anisotropy of the materials, etc.) with the information that can be extracted from the image sequence to obtain quantitative measurements. We extract shape information of the objects in the image sequence using a deformable surface matching algorithm, and characterize the changes the objects undergo using a physics-based elastic FE model.

The idea is similar to those proposed by the cardiac [46] and brain image analysis groups [33], [50], [25]; we track boundary surfaces in the image sequence, and we use the boundary motion as input for a FE model. The boundary motion is used as a boundary condition for the FE model to infer a volumetric deformation field.

The main contributions of this work are that instead of using a generic parameterized FE model that is fitted to the image data, and instead of using the pixels (or voxels) as basic elements of the FE model, we propose an algorithm for generating patient-specific tetrahedral FE models from the initial 3D image in the sequence, with locally adaptable resolution, and integrated boundary surfaces [16], [15]. Moreover, we compute the correspondences between landmark surfaces automatically using a deformable surface matching algorithm, providing us with an implicit way to compute the forces the model has undergone from one image to the next one [17], [15]. This enables us to perform all computations automatically in 3D, without manual interaction, and moreover, on a limited number of elements, with equivalent accuracy, and in a reasonable amount of time on a common workstation, thanks to an efficient implementation of the FE deformation algorithm [59].

II. Description of the Algorithm

Figure 1 presents a typical sequence of intraoperative 0.5 Tesla MR images of the brain (typically a 256x256x60 matrix where the voxel size is 0.9375x0.9375x2.5 mm^3). The three images have been aligned with an algorithm based upon mutual information (MI) [60], so as to account for patient movement within the magnet. One can very well observe the shift on the third image in the direction of the gravity, as well as the shrinking of the lateral ventricles. The aim of our algorithm will be to deform the initial image onto the last image so as to be able to transpose the surgical procedure that has been prepared preoperatively onto the target image taken during surgery when the brain has shifted.

There are two important points for doing physics-based modeling of deformations in 3D image sequences. One first needs to have a prior bio-mechanical model of the object represented by

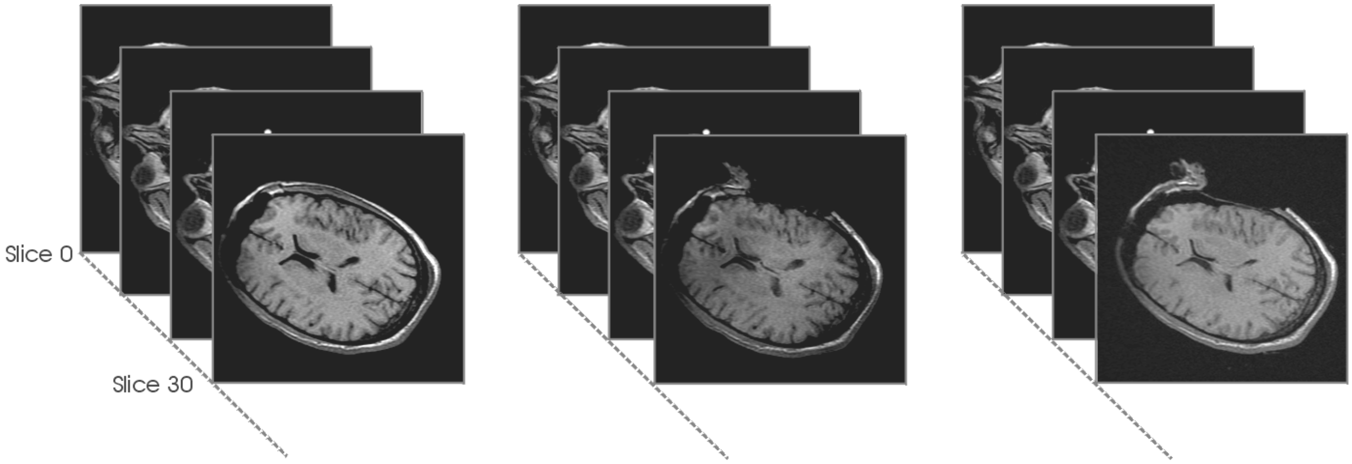

Fig. 1. Typical sequence of intraoperative MR scans. The second scan was taken just after dura removal, the third scan was taken after the brain had shifted.

the image, i.e., the constitutive equations modeling the behavior of the bodies (elastic, fluid, viscous fluid, etc.) represented in the image. On the other hand, one also needs a way of applying forces and boundary conditions to the model using the information from the image sequence.

In this work, we have chosen to model brain structures as elastic bodies, as it has been shown that soft tissue deformation can be modeled quite accurately using linear elasticity in the case of small strains [58], [19]. However, other constitutive materials such as viscous fluids, non-linear elastic bodies etc. could be integrated into our algorithm. As a first approximation, we consider that the objects that are being imaged have an isotropic, homogeneous, linear elastic behavior during deformation. The deformations will be tracked using the boundary information of the objects in the image sequence. The boundary surfaces of the initial image are deformed towards the boundaries of the next 3D image in the sequence using a deformable surface matching algorithm. The deformation field of the boundary surfaces is finally used as a boundary condition for our biomechanical model, that will be used to infer the deformation field throughout the entire volume.

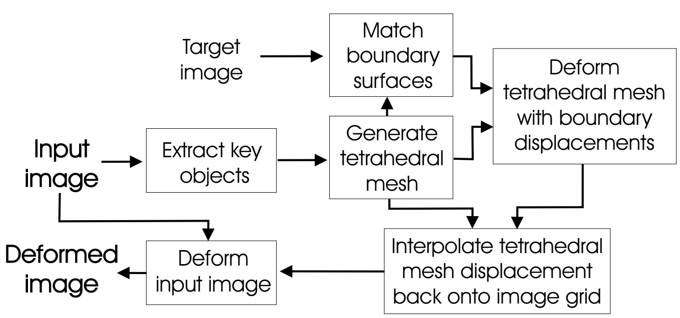

Fig. 2. Block schema of the deformable registration algorithm.

Figure 2 presents the flow diagram of our algorithm. First step is to segment the key objects out of the initial scan : the brain volume and the lateral ventricles. Next, a patient-specific multi-resolution tetrahedral mesh is generated from the brain volume, and the boundary surfaces (cortical surface, and lateral ventricular surfaces) are then deformed to match the corresponding boundaries in the target image using a deformable surface matching algorithm. The surface deformation field is then used as a boundary condition for the volumetric FE deformation model, which yields a volumetric deformation field. This deformation field is interpolated back onto the image grid using the element's shape functions. Eventually, the deformation field on the image grid is used to deform the initial image so that it matches the shape changes of the brain during surgery.

The following sections will successively review the theory of linear elasticity within a finite element modeling framework, address the FE meshing issue, and explain how we have used these principles to solve deformable surface matching problems, as well as the way we use it for computing a biomechanical volumetric deformation field. Initial experiments on two synthetic image sequences and on an actual sequence showing brain shift will also be presented.

III. Mathematical Formulation

A. Finite Elements of an Elastic Material

Assuming a linear elastic continuum with no initial stresses or strains, the deformation energy of an elastic body submitted to externally applied forces can be expressed as [62] :

$$E = \frac{1}{2}\int_{\Omega} \boldsymbol{\sigma}^T \boldsymbol{\epsilon}\, d\Omega + \int_{\Omega} \mathbf{F}\mathbf{u}\, d\Omega \qquad (1)$$

where $\mathbf{u} = \mathbf{u}(x, y, z)$ is the unknown displacement vector, $\mathbf{F} = \mathbf{F}(x, y, z)$ the vector representing the forces applied to the elastic body (forces per unit volume, surface forces or forces concentrated at the nodes), and Ω the body on which one is working. $\boldsymbol{\epsilon}$ is the strain vector, defined as

$$\begin{aligned}\boldsymbol{\epsilon} &= \left(\frac{\partial \mathbf{u}}{\partial x}, \frac{\partial \mathbf{u}}{\partial y}, \frac{\partial \mathbf{u}}{\partial z}, \frac{\partial \mathbf{u}}{\partial x} + \frac{\partial \mathbf{u}}{\partial y}, \frac{\partial \mathbf{u}}{\partial y} + \frac{\partial \mathbf{u}}{\partial z}, \frac{\partial \mathbf{u}}{\partial x} + \frac{\partial \mathbf{u}}{\partial z}\right)^T \\ &= \mathbf{L}\mathbf{u}\end{aligned} \qquad (2)$$

and $\boldsymbol{\sigma}$ the stress vector, linked to the strain vector by the constitutive equations of the material. In the case of linear elasticity, with no initial stresses or strains, this relation is described as

$$\boldsymbol{\sigma} = \left(\sigma_x, \sigma_y, \sigma_z, \tau_{xy}, \tau_{yz}, \tau_{xz}\right)^T = \mathbf{D}\boldsymbol{\epsilon} \qquad (3)$$

where $\mathbf{D}$ is the elasticity matrix characterizing the properties of the material. The matrix is symmetric, this stems from the symmetry of the stress and strain tensors [62, page 51]; thus there are 21 elastic constants for a general anisotropic material. In the case of an orthotropic material, the material has three mutually perpendicular planes of elastic symmetry [57]. Hence, there are nine unknown parameters. For a material with the maximum symmetry, i.e. an isotropic material, the material properties are the same in every direction, so there are only two independant parameters left : Young's modulus (E) which relates tension and stretch, and the Poisson ratio (ν), which is the ratio of the lateral contraction due to longitudinal stretch.

Equation 3 is valid whether one is working with a surface or a volume. We model our deformable surfaces, which represent the boundaries of the objects in the image, as elastic membranes with negigeable thickness and zero stiffness bending moments, and the surrounding and inner volumes as 3D volumetric isotropic linear elastic bodies.

Within a finite element discretization framework, an elastic body is approximated as an assembly of discrete finite elements interconnected at nodal points on the element boundaries. This means that the volumes to be modeled need to be meshed, i.e. divided into elements. Our meshing algorithm will be described in the next section.

The continuous displacement field $\mathbf{u}$ within each element is approximated as a function of the displacement at the element's nodal points $\mathbf{u}_i^{el}$ weighted by its shape functions $N_i^{el} = N_i^{el}(x, y, z)$:

$$\mathbf{u} = \sum_{i=1}^{N_{nodes}} N_i^{el} \mathbf{u}_i^{el} \tag{4}$$

The elements we use are tetrahedra ($N_{nodes} = 4$) for the volumes and triangles ($N_{nodes} = 3$) for the surfaces, with linear interpolation of the displacement field. Hence, the shape function of node i of tetrahedron or triangle el is defined as:

$$N_i^{el} = K\Big(a_i^{el} + b_i^{el}x + c_i^{el}y + d_i^{el}z\Big) \tag{5}$$

where $K = \frac{1}{6V^{el}}$ for a tetrahedron, and $K = \frac{1}{2S^{el}}$ for a triangle. The computation of V^{el}, S^{el} (volume, surface of el) and the other constants is detailed in [62, pages 91–92].

For every node i of each element el, we define the matrix $\mathbf{B}_i^{el} = \mathbf{L}_i N_i^{el}$ (where $\mathbf{L}_i$ is matrix $\mathbf{L}$ at node i, see Eq. 2). Substituting Eq. 3 and Eq. 4 in Eq. 1, the function to be minimized on each element el can thus be expressed as

$$E\big(\mathbf{u}_1^{el}, \ldots, \mathbf{u}_{N_{nodes}}^{el}\big) = \frac{1}{2}\int_\Omega \sum_{i=1}^{N_{nodes}} \sum_{j=1}^{N_{nodes}} \mathbf{u}_i^{el^T} \mathbf{B}_i^{el^T} \mathbf{D} \mathbf{B}_j^{el} \mathbf{u}_j^{el}\, d\Omega + \int_\Omega \sum_{i=1}^{N_{nodes}} \mathbf{F} N_i^{el} \mathbf{u}_i^{el}\, d\Omega \tag{6}$$

We seek the minimum of this function by solving for

$$\frac{\partial E\big(\mathbf{u}_1^{el}, \ldots, \mathbf{u}_{N_{nodes}}^{el}\big)}{\partial \mathbf{u}_i^{el}} = 0 \quad ; \quad i = 1, \ldots, N_{nodes} \tag{7}$$

Equation 6 then becomes:

$$\int_\Omega \sum_{j=1}^{N_{nodes}} \mathbf{B}_i^{el^T} \mathbf{D} \mathbf{B}_j^{el} \mathbf{u}_j^{el}\, d\Omega = - \int_\Omega \mathbf{F} N_i^{el}\, d\Omega \quad ; \quad i = 1, \ldots, N_{nodes} \tag{8}$$

This last expression can be written as a matrix system for each finite element:

$$\mathbf{K}^{el} \mathbf{u}^{el} = -\mathbf{F}^{el} \tag{9}$$

Matrices $\mathbf{K}^{el}$ and vector $\mathbf{F}^{el}$ are defined as follows.

$$\begin{cases} \mathbf{K}_{i,j}^{el} = \displaystyle\int_\Omega \mathbf{B}_i^{el^T} \mathbf{D} \mathbf{B}_j^{el}\, d\Omega \\ \mathbf{F}_i^{el} = \displaystyle\int_\Omega \mathbf{F} N_i^{el}\, d\Omega \end{cases} \tag{10}$$

where every element i, j refers to pairs of nodes of the element el (i and j range from 1 to 4 for a tetrahedron – 1 to 3 for a triangle). $\mathbf{K}_{i,j}^{el}$ is a 3 by 3 matrix, and $\mathbf{F}_i^{el}$ is a 3 by 1 vector. The 12 by 12 (9 by 9 for a triangle) matrix $\mathbf{K}^{el}$, and the vector $\mathbf{F}^{el}$ are computed for each element. The coefficients i, j of the local matrices (corresponding to a pair of nodes i, j within the local element) are summed up at the locations $g(i), g(j)$ in the global matrix (where $g(i)$ represents the number of the element's node in the entire mesh). The assembly of the local matrices then leads to a global system

$$\mathbf{K}\mathbf{u} = -\mathbf{F} \tag{11}$$

the solution of which will provide us with the deformation field corresponding to the global minimum of the total deformation energy.

The assembly and solving of the linear matrix systems have been parallelized using the Message Passing Interface (MPI) and the Portable, Extensible, Toolkit for Scientific computations (PETSc) library [2].

We now have constitutive equations that model surfaces as elastic membranes and volumes as elastic bodies.

B. Finite Element Mesh Generation

B.1 Review of Existing Algorithms for Tetrahedral Mesh Generation

In [25], Hagemann et al. propose to use the pixels of the image as basic elements of the FE mesh. This is needed in order to have an accurate representation of contours. Using larger elements would lead to inaccuracies at the boundaries due to a stair-case effect. However, when performing computations in 3D, which is eventually what is needed for medical applications, the amount of degrees of freedom will be far too large (for a typical 256x256x60 intraoperative MR image, this means about 12 million degrees of freedom at worst case !) to perform efficient computations in a reasonable time, even on high performance computing equipment. Therefore, to limit computational complexity, it is desirable to work with less elements, suggesting that one may use elements covering several image samples. For computational ease and because they yield better representations of the domains, tetrahedral elements are often chosen to represent volumes.

There are two major kinds of approaches to tetrahedral mesh generation : those based on the Delaunay criterion [12], and those based upon iso-voluming. Iso-voluming consists of clipping an initial regular subdivision along a constant intensity value (iso-value) of underlying scalar content. There are also techniques known as contour linking techniques that extract parallel contours, and try to assemble them afterwards to reconstruct surfaces or volumes. We will not consider such techniques, because they are computationally more expensive, and can be seen as a subset of the other methods. The interested reader can refer to [37] and [21] as examples.

B.1.a Delaunay Tetrahedralization. The Delaunay criterion, also called the empty sphere property, says that any node of the mesh must not be contained within the circumsphere of any tetrahedra (triangles) in the mesh [12]. This criterion has been exploited very intensively for triangular surface and volumetric tetrahedral mesh generation by P.L. Georges [22] among others (see [45] for a complete review).

Most meshing techniques using this criterion either require an initial surface representation of the object to be meshed, or a set of input nodes that are part of the output mesh. This requires a pre-processing step to extract significant boundary node positions from the image data. This process may be computationally as complex as the meshing itself. Surface based techniques tetrahedralize the object by inserting nodes into the mesh, and redefining tetrahedra locally. It is the method that is chosen for defining where to locate the interior nodes that distinguishes one Delaunay algorithm from another [45]. A potential drawback is that these algorithms often replace input nodes and change the topology of the initial surface from which the tetrahedral mesh is to be computed to satisfy the Delaunay criterion. This is not always a desired feature. The main drawback of these meshing techniques is that they often require the objects to be meshed to be convex. This can be circumvented by splitting non-convex objects into smaller convex objects, and enforcing boundary conditions at the seams between sub-objects. When only input nodes are specified, there is no direct means to specify the inside and outside of the object and if it is non-convex, the algorithm will yield a mesh contained in the convex envelope of the input data.

We tested several publicly available Delaunay-based packages ([21] and others found in [45]) on brain structures. Most of them failed, or generated an unacceptable amount of very small tetrahedra. Commercial packages can have a much more stable behaviour, but are extremely expensive.

The advantage of Delaunay based algorithms is that they provide a mesh with well-shaped elements, that can have near optimal aspect ratios (this means that the triangular facets of every tetrahedron have about the same size, with angles close to $\pi/3$).

B.1.b Octree Mesh Representation. The octree technique divides the elements (cubes, tetrahedra, etc.) of an initial volume containing the geometric model recursively until the desired resolution is reached [45]. It must be noted that the octree technique does not match a predefined surface mesh. To ensure element sizes do not change too dramatically, the maximum difference in octree subdivision level between adjacent cubes can be limited. Special care needs to be taken in order to ensure the consistency of the mesh for elements that lie next to elements that have been subdivided at a higher level.

Staadt and Gross [54] describe a method to generate an octree-like subdivision of an image into tetrahedra for doing level-of-detail volume visualization. The idea is to recursively subdivide an initial tetrahedralization of the bounding box of the image until an error limit computed by iso-surface extraction from the initial volume on the current tetrahedral mesh (using marching tetrahedra) is reached.

B.1.c Iso-voluming. Iso-voluming and iso-surfacing algorithms proceed by clipping the elements of an initial regular subdivision of the domain to be meshed along a constant value. The idea was made popular by Lorensen et al. [34] for surface reconstruction (marching cubes algorithm). The clipping of the elements of the initial subdivision is done if the element lies across a threshold (so-called iso-intensity value) crossing of underlying scalar content (e.g. gray-values of an image).

Authors from the computer graphics community have developed a set of other tools for generating tetrahedral meshes for volume visualization. The ideas are the same as those proposed for iso-surface mesh generation, but instead of only extracting boundary facets, one extracts volumetric elements and the initial volumetric elements one is marching through are also added if they are contained in the object to be meshed.

Nielson and Sung [44] have developed such an algorithm for tetrahedralizing image volumes that is a generalization of the iso-surface commonly associated with the marching cubes algorithm. The algorithm subdivides the image into hexahedra (e.g. voxels), and performs volumetric iso-contouring element by element using a pre-computed table containing the basic volumetric decomposition cases. The advantage of such a method is that it is fast and generates a very regular mesh except for the boundary elements that can have degraded aspect ratios. The main disadvantage is that the average size of the generated elements is determined by the initial size of the hexahedra into which the image is initially divided. Only the elements that have been iso-contoured are divided into smaller elements.

B.2 Our Approach

Anatomical structures often have very complex, non-convex shapes, and are not very well suited for Delaunay algorithms. Therefore, we have implemented a tetrahedral mesh generator specifically suited for labeled 3D medical images, which borrows ideas from iso-voluming and octree mesh representation. The algorithm can be seen as the volumetric counterpart of a marching tetrahedra iso-surface generation algorithm, the main difference being that the initial tetrahedralization we use can have an adaptive resolution with sizes of tetrahedra depending on the underlying image content [16], [15], [14]. The algorithm has been made computationally very cheap through the use of pre-computed subdivision case tables. The most expensive part in the algorithm is the generation of the initial multiresolution tetrahedral grid, which depends on the underlying image content.

The labeled 3D image from which the mesh needs to be computed is first divided into cubes of a given size, which are further divided into five tetrahedra with an alternating pattern so as to avoid diagonal crossings on the shared quadrilateral faces of neighboring cubes. The initial cube size determines the size of the largest tetrahedra the mesh will contain. Each tetrahedron is then checked for subdivision according to the underlying image content. In our case, we decided to only subdivide tetrahedra that lie across boundaries of given objects, so as to have a detailed description of their boundaries. The edges of those tetrahedra to be subdivided are labeled for subdivision, and a new vertex is inserted at their middle point. This process is executed iteratively until the smallest edges have reached a specified minimum size.

At each iteration, the mesh is re-tetrahedralized given the required edge subdivisions for each tetrahedron. The main problem is to re-mesh tetrahedra that lie next to tetrahedra that are being split. For those tetrahedra, only some edges have been split. The mesh is therefore re-tetrahedralized using a case table with the $2^6 = 64$ possible edge splitting configurations. There are 10 basic configurations, the others are symmetrical, as presented in Figure 3 (the gray coloring and the different node labelings are represented only to facilitate visualization of the tetrahedra's subdivisions). From upper left to lower right, Figure 3 successively presents the tetrahedralization if one edge is split, if two edges are split (2 possible configurations), if three edges are split (3 possible configurations), if 4 edges are split (3 possible configurations), if 5 edges are split and finally if all edges of the tetrahedron are split.

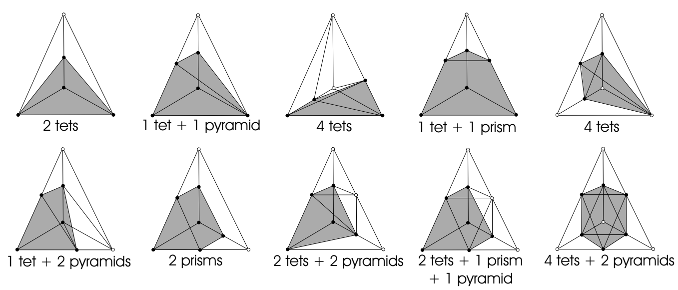

Fig. 3. Different subdivisions of a tetrahedron given edge splittings.

The resulting mesh contains tetrahedra, but also pyramids and prisms, which need to be further tetrahedralized. The main issue here is to ensure consistency[1] between the diagonals of quadrilateral faces shared by 2 elements (pyramids or prisms). We split the quadrilateral faces along the shortest diagonal so as to have better shaped tetrahedra. The subdivision of a pyramid into two tetrahedra is then straightforward given the diagonal of the quadrilateral face. For a prism, there are eight possible tetrahedralizations given the diagonal configuration. Figure 4 presents the different possible tetrahedralizations of a prism given the diagonal's configuration of the 3 quadrilateral faces. If no straight tetrahedralization is possible (cases 1 and 8), a vertex is inserted in the middle of the prism which is then divided into 8 tetrahedra.

Finally, we apply a marching tetrahedra-like clipping to generate the actual tetrahedral mesh with accurately represented boundary surfaces. For each tetrahedron, the image labels at its

[1]A consistent tetrahedral mesh is built such that every (non-boundary) triangular face is shared by exactly 2 tetrahedra.

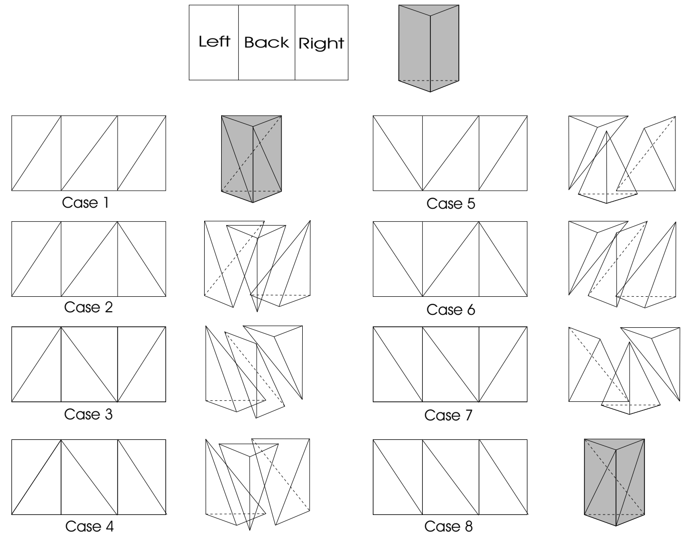

Fig. 4. Different subdivisions of a prism given the quadrilateral faces' diagonals.

nodes are checked. A case table draws the elements to be added to the mesh. If all 4 nodes have non-object labels, no tetrahedron is added to the mesh. If all nodes have an object label, the tetrahedron is added to the mesh as is. If the tetrahedron lies across two objects (i.e. all nodes do not have the same label), the subdivision of the original tetrahedron is looked up in the case table.

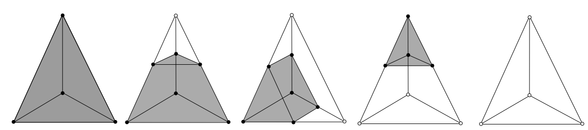

Fig. 5. Different tetrahedral clipping cases depicted from left to right. Case 1: all nodes belong to structure; case 2: 3 nodes belong to structure; case 3: 2 nodes belong to structure; case 4: 1 node belongs to structure; case 5: no nodes belong to structure.

Figure 5 shows the 5 basic configurations of the case table. There are actually 16 configurations, but the remaining ones are symmetric to cases 2, 3, and 4. The resulting prisms are divided into tetrahedra using the same approach as presented above.

The resulting mesh structure is built such that for images containing multiple objects, a fully connected and consistent tetrahedral mesh is obtained for every cell, with a given label corresponding to the object the cell belongs to. Therefore, different biomechanical properties and parameters can easily be assigned to the different cells or objects composing the mesh. Boundary surfaces of objects represented in the mesh can be extracted from the mesh as triangulated surfaces, which is very convenient for running a deformable surface matching algorithm.

Figure 6 illustrates the behavior of our algorithm on an image of a sphere. Two meshes were generated, with and without adaptive resolution of the initial grid from which the meshes were clipped along the boundaries of the sphere. The first mesh (see Figure 6a,b,c) had 2695 tetrahedra and the sphere boundary surface 344 triangular facets. The multiresolution mesh (see Figure 6d,e,f) had 43580 tetrahedra, and the boundary surface of the sphere 6958 triangular facets. The subdivision of the initial tetrahedralization of the volume allows for variable element sizes, and therefore a more accurate representation of some boundary surfaces. Note that in order to have the same accuracy for the sphere's boundary surface without adaptive subdivision of the initial mesh, the mesh would count 171114 tetrahedra, and thus lead to a higher computational load for further FE calculations.

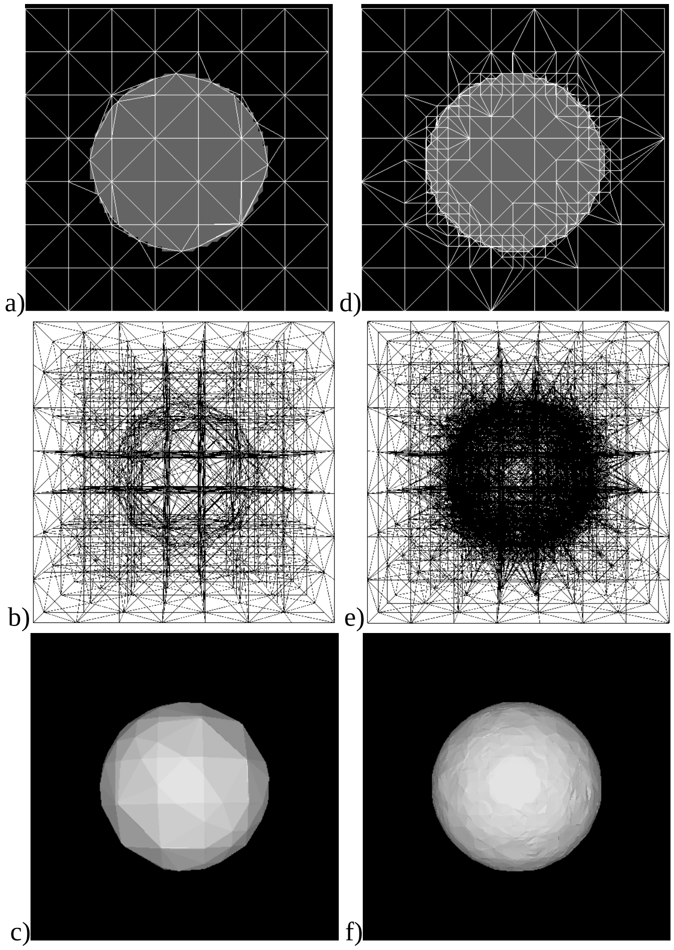

Fig. 6. Tetrahedral meshes of an embedded sphere. (a,b,c) Initial subdivision of image into cubes, followed by clipping of the sphere (2695 tetrahedra). The boundary sphere has limited resolution, but most elements have a good aspect ratio. (c,d,e) Multi-resolution subdivision of same mesh using 2 subdivision levels, followed by clipping (43580 tetrahedra). The boundary surface is more precise. (a,d) Cut through tetrahedral mesh overlayed on corresponding cut through image. (b,e) 3D renderings of wireframe of entire mesh. (c,f) 3D Surface renderings of boundary surface of the sphere.

B.3 Improvement of Mesh Quality

The quality of mesh elements can be crucial for further Finite Element analysis. A perfect tetrahedral element has triangular facets having the same size, with angles of $\pi/3$. Elements having degraded aspect ratios (e.g. one edge is much shorter than the others) have a lower quality. Poorly shaped or distorted elements can result in numerical difficulties during the solution process. For example, it has been shown that as element angles become too large, the discretization error in the finite element solution is increased and as angles become too small the condition number of the element matrix is increased [18]. Thus, for meshes containing distorted elements, the numerical solution is more difficult to compute and the numerical approximation is less accurate. Most tetrahedral quality measures are based on geometric quality indicators [48], [3]. One common example is the so-called aspect ratio, defined as

$$A_\gamma = \frac{\left(\frac{1}{6}\sum_{i=1}^{6} l_i^2\right)^{3/2}}{8.47867V^{el}} \quad (12)$$

where V^{el} is the volume of the tetrahedron, and l_i $(i = 1, ..., 6)$ are its edge lengths. The aspect ratio metric is normalized so that $A_\gamma = 1$ corresponds to an ideal element and $A_\gamma \longrightarrow \infty$ as the element becomes increasingly distorted.

To improve the shape of those elements that had distorted shapes, we have implemented a simple laplacian smoothing algorithm, and applied it in the second order neighborhood (i.e. up to two edges away) of all the tetrahedra having a degraded aspect ratio. Laplacian smoothing relocates grid points to the mean of their incident vertices to improve mesh quality without changing mesh topology. The laplacian smoothing is applied iteratively, by ensuring that the smoothing is not degrading other element's shapes at every iteration, improving the elements aspect ratio (see Eq. 12) and without moving the boundary surface nodes.

C. *Validation of the FE Elastic Deformation Model*

In this section, we assess the computational integrity of our FE implementation on a problem with a known analytical solution. A cube fixed on its bottom face is deformed with a uniform force distributed on the top face. The deformation is computed on meshes with decreasing mesh qualities, and the calculated node positions are compared against the expected analytical result.

Table III-C reports the results for a cube of 63x63x63mm, whose top face is loaded with a uniform force producing a downwards displacement of 10 mm in the downwards direction. The quality of the meshes was degraded by clipping elements around the boundaries of an embedded sphere (i.e. as in Figure 6a,d). The results reported here are for an isotropic homogeneous elastic material, whose Poisson ratio was $\nu = 0.45$ and Young's modulus $E = 1kPa$. Similar results were obtained for different material parameters.

TABLE I

FINITE ELEMENT (FE) DISCRETIZATION ERROR ANALYSIS FOR CUBE LOADING EXPERIMENT. EDGE LENGTHS (AVERAGE : $\overline{l_i}$, MINIMUM : l_i^{min}, MAXIMUM : l_i^{max}) AND FINITE ELEMENT DISCRETIZATION ERRORS (AVERAGE : $\overline{Err}$ AND MAXIMUM : Err^{max}) ARE MEASURED IN MM. THE AVERAGE ASPECT RATIOS ($\overline{A_\gamma}$) ARE MEASURED USING EQUATION 12. MESH 1 HAS 16875 TETRAHEDRA, MESH 2 HAS 20287 TETRAHEDRA, AND MESH 3 HAS 57199 TETRAHEDRA.

	$\overline{l_i}$	l_i^{min}	l_i^{max}	$\overline{A_\gamma}$	$\overline{Err}$	Err^{max}
1	5.04	5.94	4.19	1.29	1.6×10^{-6}	1×10^{-4}
2	4.71	0.03	5.94	13.85	1.8×10^{-5}	8×10^{-3}
3	2.94	0.03	5.94	16.2	6.3×10^{-5}	1×10^{-2}

This experiment illustrates that the error induced by the FE discretization of the elasticity equations is not a significant source of error for our application, even for meshes with degraded aspect ratios.

D. Deformable Surface Matching Algorithm

The deformable surface matching algorithm deforms the boundary surface of an object in one volumetric scan of the sequence towards the boundary of the same object in the next scan of the sequence. This is done iteratively by applying image-derived forces $\mathbf{F}^{\mathbf{v}^t}$ (forces computed using the surface's nodal positions $\mathbf{v}$ at iteration t) to the elastic surface. The surface is modeled using the equations presented above (see Eq. 11). The temporal variation of the surface can be discretized using finite differences, provided the time step τ is small enough [8]. This yields the following semi-implicit iterative equation :

$$\frac{\mathbf{v}^t - \mathbf{v}^{t-1}}{\tau} + \mathbf{K}\mathbf{v}^t = -\mathbf{F}^{\mathbf{v}^{t-1}} \tag{13}$$

which can be rewritten as :

$$\big(\mathbf{I} + \tau\mathbf{K}\big)\mathbf{v}^t = \mathbf{v}^{t-1} - \tau\mathbf{F}^{\mathbf{v}^{t-1}} \tag{14}$$

The external forces driving the elastic membrane towards the edges of the structure in the image are integrated over each element of the mesh and distributed over the nodes belonging to the element using its shape functions (see Eqn. 4). Classically, the image force $\mathbf{F}$ is computed as a decreasing function of the gradient so as to be minimized at the edges of the image [31], [8]. A potential weakness of surface matching methods is that for correct convergence, the surfaces need to be initialized very close to the edges of the object to be segmented. Cohen and Cohen [8] propose to use inflation or deflation forces (so-called balloon forces) to circumvent that problem and increase the capture range of the deformable surface. Xu and Prince [61] compute the force field driving the curve separately on the segmented target image by solving a separate second order differential equation coming from electromagnetics. The main disadvantage of such an approach is that it is computationally prohibitive in 3D. To increase the robustness and the convergence rate of the surface deformation, we compute the forces as a gradient descent on a euclidean distance map of the edges in the target image. The distance map is computed very efficiently using a fast distance transformation algorithm [10], [9].

This yields the following relation for the external force :

$$\mathbf{F}(\mathbf{x}) = S_{min}\nabla\Big(\mathcal{D}\big(I(\mathbf{x})\big)\Big) \tag{15}$$

where $\mathcal{D}\big(I(\mathbf{x})\big)$ represents the distance transformation of the target image at point $\mathbf{x}$. S_{min} is chosen so that the gradient points towards a point with a smaller distance value :

$$S_{min} = \begin{cases} +1 & \text{if} \quad \mathcal{D}\big(I(\mathbf{x})\big) > \mathcal{D}\Big(I\big(\mathbf{x} + \nabla\big(\mathcal{D}\big(I(\mathbf{x})\big)\big)\big)\Big) \\ -1 & \text{if} \quad \mathcal{D}\big(I(\mathbf{x})\big) < \mathcal{D}\Big(I\big(\mathbf{x} + \nabla\big(\mathcal{D}\big(I(\mathbf{x})\big)\big)\big)\Big) \end{cases}$$

The surface is deformed iteratively until it has reached a minimum energy specified by the user, which can be computed by integrating the distances over the surface at each iteration, or until the surface stabilizes, i.e. there are no significant deformation forces so that the surface does not deform anymore.

E. Inferring Volumetric Deformations From Surface Deformations

The deformation field obtained for the boundary surfaces is then used in conjunction with the volumetric model to infer the deformation field inside and outside the boundary surfaces.

The idea is to apply forces to the boundary surfaces that will produce the same displacement field at the boundary surfaces that was obtained with the deformable surface matching algorithm. The volumetric biomechanical model will then compute the deformation of the surrounding nodes in the mesh.

Let $\widetilde{\mathbf{u}}$ be the vector representing the displacement to be imposed at the boundary nodes. The elements of the rows of the rigidity matrix $\mathbf{K}$ corresponding to the nodes for which a displacement is to be imposed need to be set to zero, and the diagonal elements of these rows to one. The force vector $\mathbf{F}$ is then set to be equal to the displacements vector for the boundary nodes: $\mathbf{F} = \widetilde{\mathbf{u}}$ [62], [50]. This way, solving Eq. 11 for the unknown displacements will produce a deformation field over the entire FE mesh model that matches the prescribed displacements at the boundary surfaces. This volumetric displacement field is then interpolated back onto the image grid using the shape functions of every element of the mesh (see Eqn. 4) [62].

IV. Experiments

A. Synthetic Image Sequences

A.1 Embedded Sphere to Ellipsoid Experiment

In this section, we test our algorithm on a sequence of two 3D images of an elastic sphere being squeezed onto an ellipsoid [14]. The sphere has a radius of 19mm ($E = 1kPa, \nu = 0.45$), and is embedded in a cube of 63x63x63mm ($E = 10kPa, \nu = 0.45$).

A cut through the initial tetrahedral mesh of the sphere and the corresponding image are shown in Figure 7a. The original deformable surface extracted from the volumetric tetrahedral mesh is depicted in Figure 7c. Note that for this experiment, the initial tetrahedralization from which the mesh was computed was not multi-resolution, it had constant tetrahedral sizes before the volumetric marching tetrahedra contouring was applied. When running the deformable surface matching algorithm, the surface readily converges to the boundary of the ellipsoid in the target image (see Figure 7d). The corresponding cut through the volumetric tetrahedral mesh after deformation is shown in Figure 7b.

Figure 8 analyzes the deformation field resulting from matching the sphere onto the ellipsoid. The squeezing of the sphere, pulling and pushing the surrounding material around the target boundary surface can very well be observed on the 3D cuts through the deformed volume (as illustrated in Figure 8b). The deformation field (downsampled in Figure 8a) also illustrates the squeezing onto the ellipsoid.

A.2 Embedded Translated Cube Experiment

In this experiment, the aim is to match a hard isotropic elastic cube (edges of the cube have a length of $15\ mm$, $E = 100kPa, \nu = 0$) embedded in a larger soft isotropic elastic cube (edges have a length of $63\ mm$, $E = 1kPa, \nu = 0.4$) onto a target cube of the same size, but whose smaller cube has been

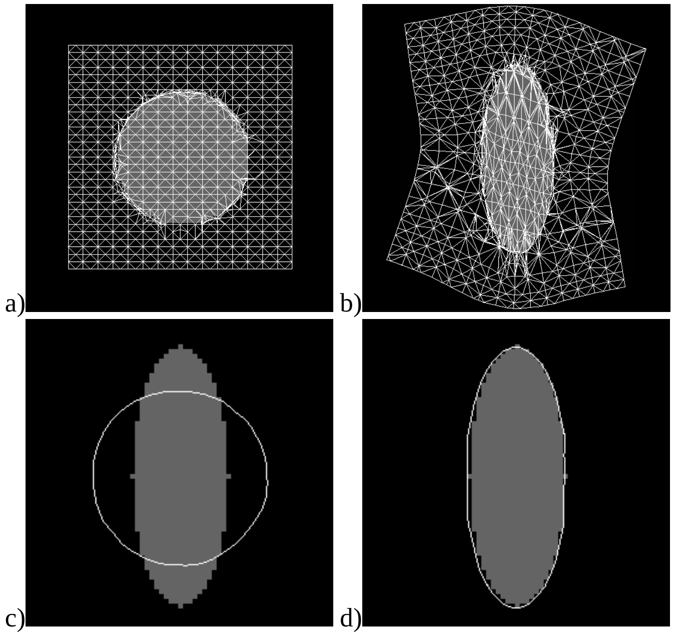

Fig. 7. Illustration of the sphere to ellipsoid matching experiment on 2D cuts. a) Cut through initial image with corresponding cut through initial volumetric mesh, b) same cut through deformed volumetric mesh on target image. c) Initial sphere boundary surface overlayed on corresponding cut through target image, d) same as in c) but after deformation of initial sphere boundary surface on target image.

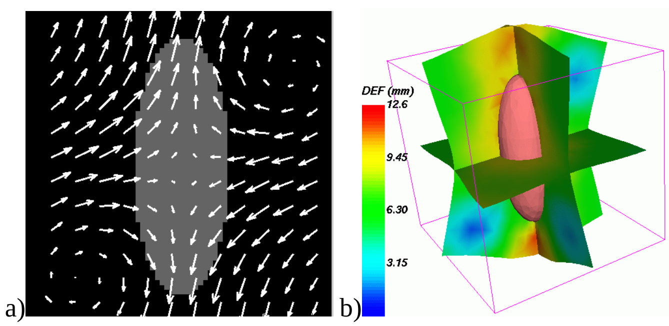

Fig. 8. Analysis of the deformation field resulting from sphere to ellipsoid matching. a) The deformation field overlayed on cut through target image of ellipsoid. b) Orthogonal cuts through the deformed volumetric mesh, illustrating the squeezing of the sphere and the surrounding elastic medium onto the ellipsoid. The color-coding reflects the norm of the deformation vectors.

translated by a vector of $(-5mm, -5mm, -5mm)$. The boundary surface of the larger cube is assumed not to move, that of the smaller cube is translating within the larger one.

Figure 9a presents a cut through the initial tetrahedral mesh overlayed on the corresponding cut through the image representing the first cube. Again, in this experiment, the initial mesh had not been adaptively refined before clipping the elements lying across image boundaries. Figure 9c,d represent the boundary surface of the smaller cube overlayed on the target image, before and after surface matching. In this experiment, we used a distance transform based rigid registration algorithm to correct for the translation [14]. The active surface algorithm alone would not have been able to recover such a large translation. The boundary displacement of the smaller cube is then used as input to the volumetric FE model, which is then deformed. Figure 9b shows the same cut as in sub-figure 9a through the deformed mesh overlayed on the corresponding cut through the target image.

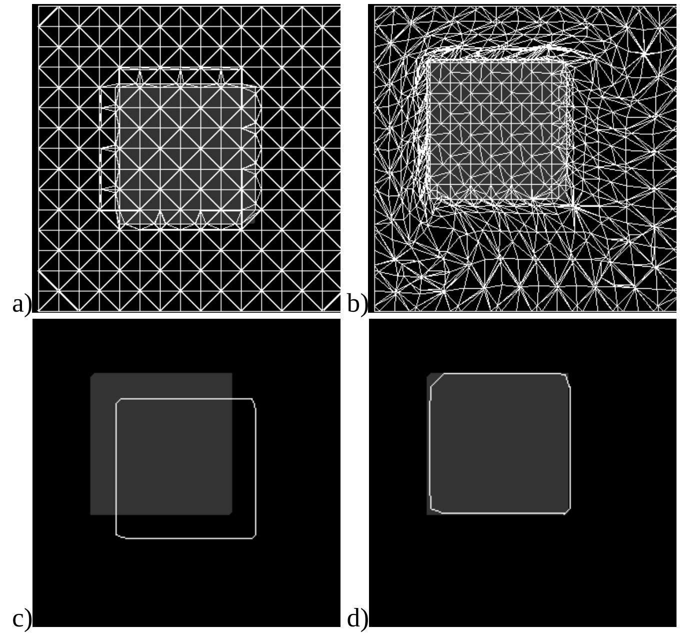

Fig. 9. Translated cube experiment. a) Cut through initial volumetric tetrahedral mesh overlayed on corresponding cut through image the mesh was generated from. b) Cut through deformed FE mesh overlayed on cut through target image. c) Cut through initial boundary surface overlayed on corresponding cut through target image. d) Cut through deformed boundary surface (after affine transformation) overlayed on corresponding cut through target image. This illustrates the rigid translation of the cube, pulling tissue of the lower right corner and compressing the soft tissue in the upper left corner.

Figure 10a shows orthogonal cuts through the deformed mesh with color-coding of the intensity of the deformation field with the actual 3D deformation field. Figure 10b shows the 2D deformation field interpolated back onto the image grid and overlayed on corresponding cut through the initial image.

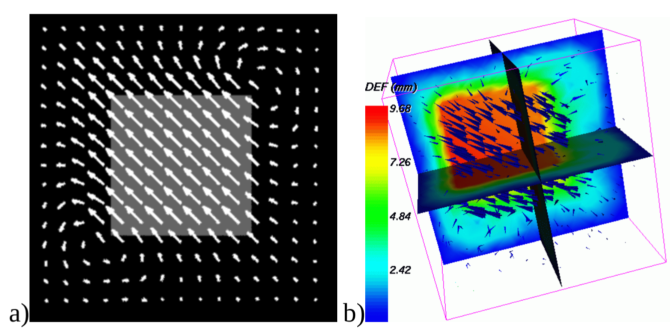

Fig. 10. Translated cube experiment. a) 2D deformation field overlayed on cut through initial image. b) 3D rendering of cuts through deformed FE mesh with arrows representing the actual 3D deformation field. Color-coding corresponds to the intensity of the deformation. The deformation field is translational within the hard cube, and has a rotational component in the soft part towards the edges of the image boundaries.

This experiment illustrates how the translation of the smaller cube within the larger compresses and stretches the soft object the smaller cube is embedded in.

B. Brain Shift Analysis

In this section, we apply our algorithm to the two intraoperative MR scans of the brain acquired before surgery had started and after removal of the dura (scans 1 and 3 in Figure 1). Before we applied our algorithm on the brain shift images, we aligned them using a rigid registration algorithm based upon maximization of mutual information [60] so as to account for patient movement within the magnet during the operation. All the steps of the algorithm are carried out once the images have been aligned.

B.1 Material Properties

An isotropic linear elastic material is characterized by two parameters: Young's elasticity modulus E and Poisson's ratio ν [62]. They determine the elastic behavior of the object. The choice of these values is of course critical to the reliability of a physics based deformation model. Their determination has not been addressed very consistently in the literature as the coefficients used often differ significantly from study to study and do not always include the physical units of the values. Recently, Hagemann et al.[25] published a comparative study of brain elasticity coefficients proposed by different authors, and came to the conclusion that for their application, the only comparable and meaningful values presented by other authors are the ratios of the coefficients for brain and skull. Since we are only interested in modeling the brain, and not the skull, we have chosen to use parameters similar to those Miga et al. [38] obtained with in-vivo experiments instead ($E = 3kPa, \nu = 0.45$).

B.2 FE Model Generation

To build our brain model, we segmented the brain out of the initial intraoperative MRI using a directional watershed algorithm [55]. The volume was further simplified using mathematical morphology to obtain a smooth surface. Figure 11 shows cuts through a sample tetrahedral mesh of the brain overlayed on the corresponding initial image. Note that the mesh has been adaptively refined only in the neighborhood of the lateral ventricles, so as to ensure sufficient resolution of the surfaces for the deformable surface matching algorithm. The average size of the edges of the larger tetrahedra was approximately 10 mm, while the smallest tetrahedra (in the neighborhood of the ventricles) had edges of 1 mm. However, it must be noted that the meshing algorithm yields even smaller tetrahedra in the neighborhood of boundary edges.

B.3 Deformable Surface Matching

The deformable surfaces are extracted from the mesh generated from the intraoperative scan at the start of surgery, before opening the dura mater (see Figure 12a), and deformed towards the brain in a later intraoperative image (see Figure 12b,c). One can very clearly observe that the deformation of the cortical surface is happening in the direction of gravity and is mainly located where the dura was removed. Also, one can observe a shift, as well as a contraction of the lateral ventricles. Figure 14 shows the 3D surface deformation field the brain and the ventricles have undergone. One can very well observe that the shift is mainly affecting the left part of the ventricles, while the displacement of the lower parts is mostly due to volume loss.

B.4 Volumetric FE Deformation

The deformation field obtained with the deformable surface matching algorithm is then used as input for our biomechanical FE model. The algorithm yields a deformation vector for every node of the mesh. These displacements can then be interpolated back onto the image grid using the shape functions within every element of the FE mesh (see Eq. 4).

Figure 13 shows a slice of the deformed image as well as the image of the difference with the target. One can observe that the algorithm captured the surface shift and the ventricular thinning very accurately. The gray-level mean square difference between the target scan and the deformed original scan on the image regions covered by the mesh went down from 15 to 3. However, one can also notice that the left ventricle (lower one in the Figure) was not able to fully capture the thinning. This is due to the approximate model of the lateral ventricles we used in this experiment.

Figure 15 shows orthogonal cuts through the target intraoperative scan with transparently overlayed color-coding of the intensity of the deformation field. The arrows show the actual displacement of the nodes of the mesh. The extremely dense vector field in the neighborhood of the lateral ventricles is due to the adaptive refinement of the mesh at these locations.

Figure 16a shows the obtained deformation field overlayed on a slice of the initial scan, and Figure 16b shows the same slice of the initial scan deformed with the obtained deformation field. Several landmarks have also been placed on the initial scan (green crosses) and deformed onto the target scan (red crosses), and these last landmarks have also been overlayed on the target scan for comparison with the actual deformed anatomy.

Similar landmarks as those shown in Figure 16 have been placed on 4 different slices where the shift was most visible, and the distance between deformed landmarks and target landmarks (not represented here for better visibility) has been measured. The surface based landmarks on the deformed scan were within 1mm of the landmarks on the target intraoperative scan. The errors between the landmarks placed in between the mid-sagittal plane and the cortical surface were within 2-3mm from the actual landmarks. The largest errors were observed at the level of the mid-sagittal plane and ventricles, which can be explained by the fact that the surface matching of the ventricles was not perfect. Nevertheless, the algorithm reduced the distance between landmarks in the initial and the target scans from up to almost 10mm to less than 1mm for the surface-based landmarks, and from up to 6mm to 3mm or less for the sub-surface landmarks.

V. Conclusions

We have presented a new algorithm for tracking and characterizing shape changes in 3D image sequences of physics-based objects. The algorithm incorporates a biomechanical model of the deforming objects and uses image-based information to drive the deformation of our model through a deformable surface matching algorithm.

The main contributions of this paper are an improved algorithm for generating multi-resolution patient-specific FE meshes

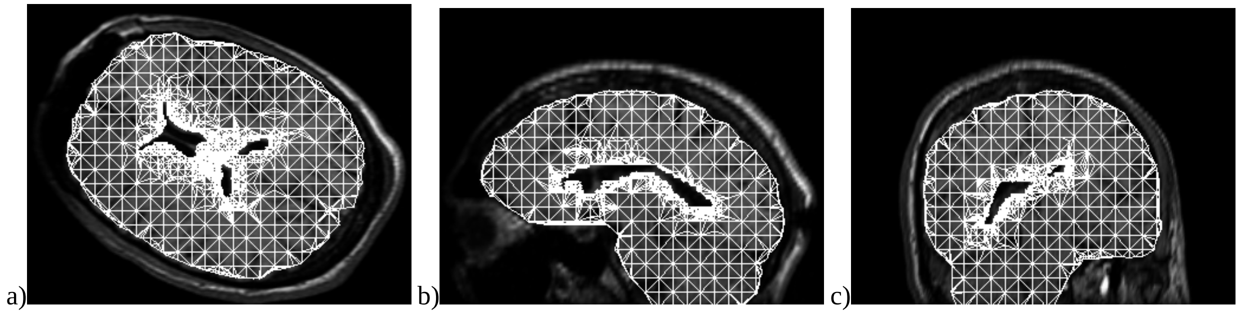

Fig. 11. Axial (a), sagittal (b), and coronal (c) cuts through tetrahedral mesh of the brain overlayed on corresponding cuts through preoperative image.

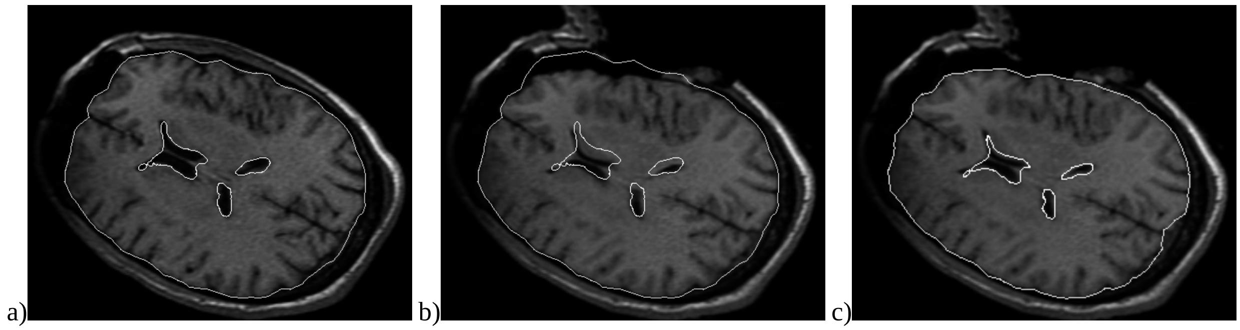

Fig. 12. Axial cut through initial (a,b) and deformed (c) deformable surfaces overlayed on corresponding slice of initial (a) and target (b,c) intraoperative MR image.

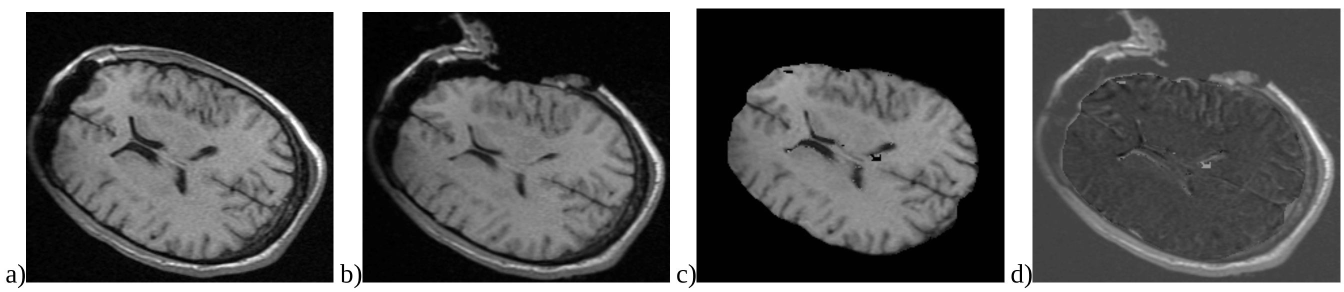

Fig. 13. Axial slice of a) initial scan b) target scan c) initial scan deformed using our algorithm (only the brain has been deformed) d) difference between target scan and deformed initial scan (gray reflects no difference).

from labeled 3D images, a deformable surface matching algorithm that automatically computes correspondences between the boundaries of 3D objects in an image sequence, and the demonstration that in conjunction with a biomechanical model, the entire algorithm is an accurate solution for the physics-based registration of preoperative images with intraoperative images of the brain. The entire deformation algorithm, using a mesh with approximately one hundred thousand tetrahedra, only takes about 30 minutes on a Sun Ultra 10 440MHz workstation. Using a parallel machine, the computation time can be reduced to a few minutes [59], which makes it suitable for use during surgery.

We believe the algorithm is promising for the analysis of 3D medical image sequences. It will provide physicians with a tool for measurement and physical interpretation of deformation in 3D image sequences, and can thus be of great aid in in the interpretation and diagnosis of these images.

Future developments include the development of a more complete biomechanical model, i.e. by including anisotropy, as well as new structures such as the falx for the brain. Also, we plan to use this algorithm on a full image sequence acquired during a neurosurgical procedure including tumor resection as well.

Acknowledgments

This work was funded in part by NIH P41 RR13218, NIH P01 CA67165, NIH R01 RR11747, NIH R01-CA86879 and a New Concept Award from the Center for Integration of Medicine and Innovative Technology (SKW). MF was supported in part by a grant from the Belgian FRIA (Fonds pour la Recherche dans l'Industrie et l'Agriculture) and the EMIM-2 project from the Région Wallonne. We thank Peter McL. Black for the opportunity and his patience, that enabled us to acquire the data necessary for our study.

References

[1] R. Bajcsy and S. Kovacic. Multi-resolution Elastic Matching. *Computer Vision, Graphics, and Image Processing*, 46:1–21, 1989.

[2] S. Balay, K. Buschelman, W. D. Gropp, D. Kaushik, L. C. McInnes, and B. F. Smith. PETSc home page. http://www.mcs.anl.gov/petsc, 2001.

[3] M. Berzins. Mesh quality : A function of geometry, error estimates or both? *Engineering With Computers*, 15(3):236–47, 1999.

[4] M. Bro-Nielsen and C. Gramkow. Fast Fluid Registration of Medical Im-

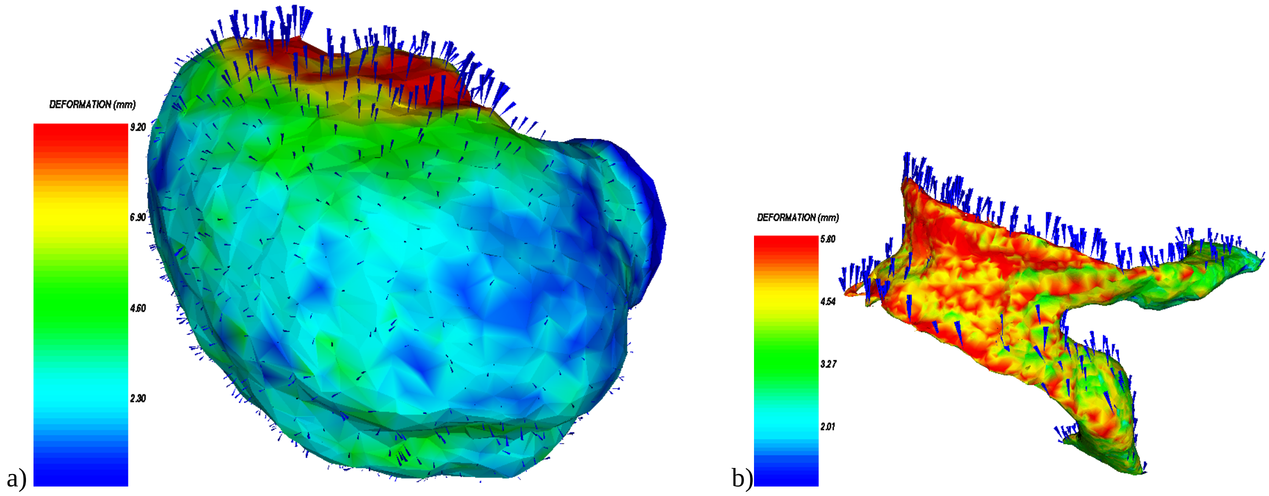

Fig. 14. 3D surface renderings of deformable surfaces with color-coded intensity of the deformation field. a) brain surface, b)lateral ventricles.

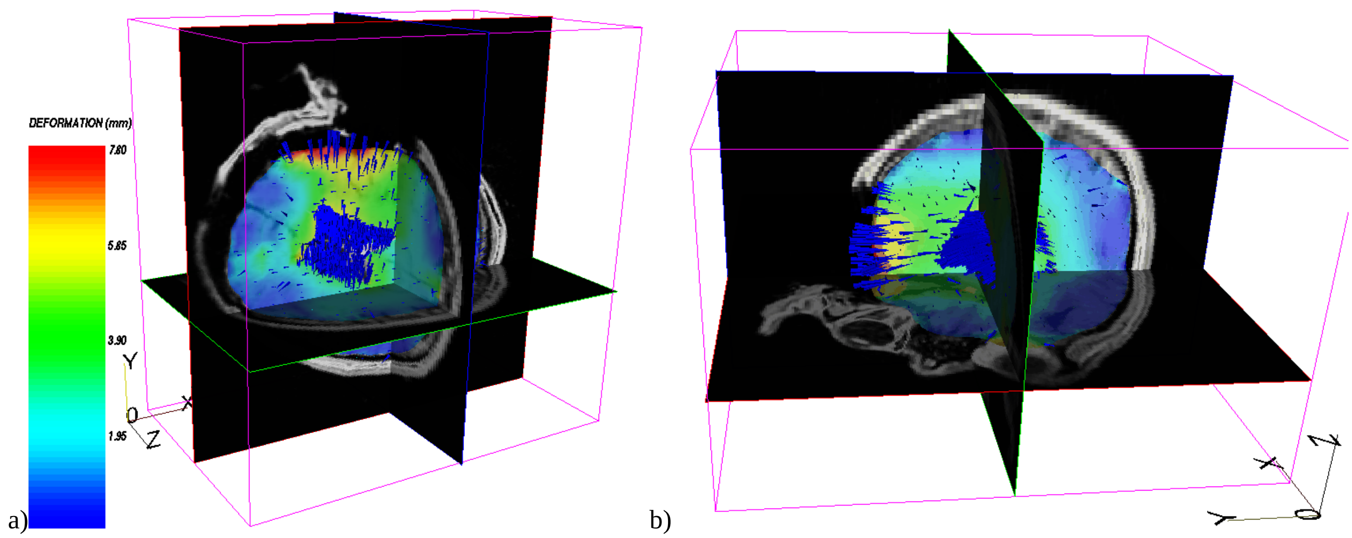

Fig. 15. 3D Volumetric Deformation field (downsampled 12x, scaled 2x) with orthogonal cuts through target intraoperative MR image and transparently overlayed color coded intensity of the deformation field. a)Axial view, gravity is downwards. b)Coronal view, gravity goes from left to right.

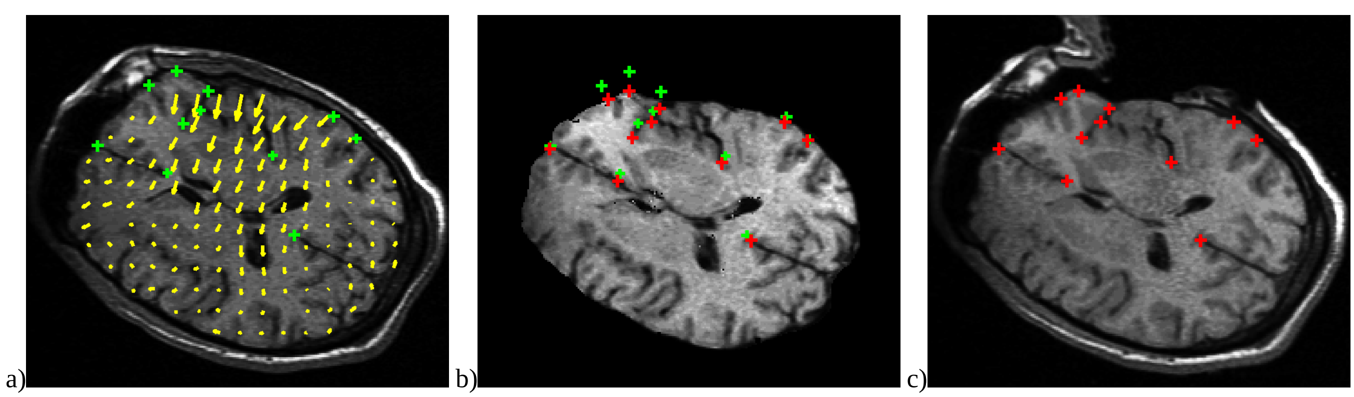

Fig. 16. a)Volumetric deformation field and initial landmarks (green) overlayed on initial intraoperative image slice. b) Same slice of deformed initial image with deformed initial landmarks (red). c) Same slice of target image with deformed landmarks.

ages. In *Visualization in Biomedical Computing (VBC '96)*, pages 267–276, 1996.

[5] C. Broit. *Optimal Registration of Deformed Images*. PhD thesis, Computer and Information Science Department, University of Pennsylvania, PA, 1981.

[6] R. D. Bucholz, D. D. Yeh, J. Trobaugh, L. L. McDurmont, C. D. Sturm, C. Baumann, J. M. Henderson, A. Levy, and P. Kessman. The Correction of Stereotactic Inaccuracy Caused by Brain Shift Using an Intraoperative Ultrasound Device. In J. Troccaz, E. Grimson, and R. Mösges, editors, *CVRMed-MRCAS '97*, pages 459–466. Springer-Verlag, Berlin, 1997.

[7] G. E. Christensen, S. C. Joshi, and M. I. Miller. Volumetric Transformation of Brain Anatomy. *IEEE Trans. Med. Imag.*, 16(6):864–877, December 1997.

[8] L. D. Cohen and I. Cohen. Finite Element Methods for Active Contour Models and Balloons for 2D and 3D Images. *IEEE Trans. Pattern Anal. and Machine Intell.*, 15:1131–1147, 1993.

[9] O. Cuisenaire. *Distance Transformations : Fast Algorithms and Applications to Medical Image Processing*. PhD thesis, Telecommunications Laboratory, Université catholique de Louvain, B-1348 Belgium, 1999.

[10] O. Cuisenaire and B. Macq. Fast Euclidean Distance Transformation by Propagation Using Multiple Neighborhoods. *Comp. Vision Image Understanding*, 76(2):163–172, 1999.

[11] C. Davatzikos. Spatial Transformation and Registration of Brain Images Using Elastically Deformable Models. *Comp. Vision Image Understanding*, 66(2):207–222, May 1997.

[12] B. N. Delaunay. Sur la Sphère Vide. In *Bul. Acad. Sci. URSS, Class. Sci Nat.*, pages 793–800, 1934.

[13] P. J. Edwards, D. L. G. Hill, J. A. Little, and D. J. Hawkes. A Three-component Deformation Dodel for Image-guided Surgery. *Med. Image Anal.*, 2(4):355–367, 1998.

[14] M. Ferrant. *Physics-based Deformable Modeling of Volumes and Surfaces for Medical Image Registration, Segmentation and Visualization.* PhD thesis, Telecommunications Laboratory, Université catholique de Louvain, B-1348 Belgium, April 2001. http://www.tele.ucl.ac.be/PEOPLE/mat/thesis.html.

[15] M. Ferrant, B. Macq, A. Nabavi, and S. K. Warfield. Deformable Modeling for Characterizing Biomedical Shape Changes. In G. Borgefors, I. Nyström, and G. Sanniti di Baja, editors, *DGCI2000 : Discrete Geometry for Computer Imagery Conference*, volume 1953, pages 235–248. Springer, December 2000.

[16] M. Ferrant, S. K. Warfield, C. R. G. Guttman, R. V. Mulkern, F. A. Jolesz, and R. Kikinis. 3D Image Matching Using a Finite Element Based Elastic Deformation Model. In C. Taylor and A. Colchester, editors, *MICCAI 99: Second International Conference on Medical Image Computing and Computer-Assisted Intervention; October 1999; Cambridge, England.*, pages 202–209. Springer, 1999.

[17] M. Ferrant, S. K. Warfield, A. Nabavi, B. Macq, F. A. Jolesz, and R. Kikinis. Registration of 3D Intraoperative MR Images of the Brain Using a Finite Element Biomechanical Model. In A. M. DiGioia and S. Delp, editors, *MICCAI 2000: Third International Conference on Medical Robotics, Imaging And Computer Assisted Surgery; 2000 Oct 11–14; Pittsburgh, USA*, pages 19–28. Springer, 2000.

[18] L. Freitag and C. Ollivier-Gooch. A Comparison of Tetrahedral Mesh Improvement Techniques. In *Proceedings of the Fifth International Meshing Roundtable*, pages 87–100, 1996.

[19] Y. C. Fung. *Biomechanics: Mechanical Properties of Living Tissues*. Springer-Verlag, Berlin, Germany, 1993.

[20] J. Gee, M. Reivich, and R. Bajcsy. Elastically Deforming 3D Atlas to Match Anatomical Brain Images. *Journal of Computer Assisted Tomography*, 17(2):225–236, 1993.

[21] B. Geiger. Three Dimensional Modeling of Human Organs and its Application to Diagnosis and Surgical Planning. Technical Report 2105, INRIA, Sophia-Antipolis, France, 1993.

[22] P.-L. Georges. Automatic Mesh Generation and Finite Element Computation. In P. Ciarlet and J. Lions, editors, *Handbook of Numerical Analysis (Part 2) Finite Element methods, Numerical Methods for Solids*, volume IV, pages 69–190. North Holland, 1996.

[23] E. Haber, D. N. Metaxas, and L. Axel. Motion Analysis of the Right Ventricle from MR Images. In *MICCAI 98: First International Conference on Medical Image Computing and Computer-Assisted Intervention; 1998 Oct 11–13; Boston, USA.*, pages 177–188. Springer, October 1998.

[24] A. Hagemann, K. Rohr, and H. S. Stiehl. Biomechanically based simulation of brain deformations for intraoperative image correction: coupling of elastic and fluid models. In K. M. Hanson, editor, *Medical Imaging 2000 - Image Processing (MI'00)*, pages 658–667, San Diego, USA, 2000. SPIE.

[25] A. Hagemann, K. Rohr, H. S. Stiel, U. Spetzger, and G. J. M. Biomechanical Modeling of the Human Head for Physically Based, Non-Rigid Image Registration. *IEEE Trans. Med. Imag.*, 18(10):875–884, October 1999.

[26] N. Hata. *Rigid and Deformable Medical Image Registration for Image-guided Surgery*. PhD thesis, Tokyo University, 1998.

[27] N. Hata, A. Nabavi, W. M. Wells III, S. K. Warfield, R. Kikinis, P. M. Black, and F. A. Jolesz. Three-Dimensional Optical Flow Method for Measurement of Volumetric Brain Deformation from Intraoperative MR Images. *Journal of Computer Assisted Tomography*, 24:531–538, 2000.

[28] D. Hill, C. Maurer, R. Maciunas, J. Barwise, J. Fitzpatrick, and M. Wang. Measurement of Intraoperative Brain Surface Deformation Under a Craniotomy. *Neurosurgery*, 43(514–526), 1998.

[29] D. L. G. Hill, C. R. Maurer, A. J. Martin, S. Sabanathan, W. A. Hall, D. J. Hawkes, D. Rueckert, and C. L. Truwit. Assessment of Intraoperative Brain Deformation using Interventional MR Imaging. In C.Taylor and A.Colchester, editors, *MICCAI 99: Second International Conference on Medical Image Computing and Computer-Assisted Intervention; October 1999; Cambridge, England.*, pages 910–919. Springer, 1999.

[30] F. A. Jolesz. Image-Guided Procedures and the Operating Room of the Future. *Radiology*, 204:601–612, May 1997.

[31] M. Kass, A. Witkin, and D. Terzopoulos. Snakes: Active Contour Models. *International Journal of Computer Vision*, 1(4):321–331, 1988.

[32] M. Knauth, C. R. Wirtz, V. M. Tronnier, N. Aras, S. Kunze, and K. Sartor. Intraoperative MR Increases the Extent of Tumor Resection in Patients with High-grade Gliomas. *Am. J. Neuroradiol.*, 20(9):1642–1646, 1999.

[33] S. K. Kyriacou, C. Davatzikos, S. J. Zinreich, and R. N. Bryan. Nonlinear Elastic Registration of Brain Images with Tumor Pathology Using a Biomechanical Model. *IEEE Trans. Med. Imag.*, 18(7):580–592, july 1999.

[34] W. E. Lorensen and H. E. Cline. Marching Cubes: a High Resolution 3D Surface Construction Algorithm. In *Computer Graphics (SIGGRAPH '87)*, volume 21, pages 163–169, 1987.

[35] C. R. Maurer, D. L. G. Hill, A. J. Martin, H. Liu, M. McCue, D. Rueckert, L. D., W. A. Hall, R. E. Maxwell, D. J. Hawkes, and C. L. Truwit. Investigation of Intraoperative Brain Deformation using a 1.5 Tesla Interventional MR System: Preliminary Results. *IEEE Trans. Med. Imag.*, 17:817–825, 1998.

[36] D. M. Metaxas. *Physics-Based Deformable Models: Applications to Computer Vision, Graphics and Medical Imaging*. Kluwer Academic Publishers, 1997.

[37] D. Meyers, S. Skinner, and K. Sloan. Surfaces from Contours. *ACM Trans. Graphics*, 11(3):228–258, 1992.

[38] M. I. Miga, K. D. Paulsen, P. J. Hoopes, F. E. Kennedy, A. Hartov, and D. W. Roberts. In Vivo Quantification of a Homogeneous Brain Deformation Model for Updating Preoperative Images During Surgery. *IEEE Trans. Med. Imag.*, 47(2):266–273, February 2000.

[39] M. I. Miga, K. D. Paulsen, J. M. Lemery, S. D. Eisner, A. Hartov, F. E. Kennedy, and D. W. Roberts. Model-Updated Image Guidance: Initial Clinical Experiences with Gravity-Induced Brain Deformation. *IEEE Trans. Med. Imag.*, 18(10):866–874, October 1999.

[40] M. I. Miga, D. W. Roberts, F. E. Kennedy, L. A. Platenik, A. Hartov, K. E. Lunn, and K. D. Paulsen. Modeling of Retraction and Resection for Intraoperative Updating of Images. *Neurosurgery*, 49:75–85, July 2001.

[41] K. Miller. Constitutive Model of Brain Tissue Suitable for Finite Element Analysis of Surgical Procedures. *Journal of Biomechanics*, 32:531–537, 1999.

[42] K. Miller, K. Chinzei, G. Orssengo, and P. Bednarz. Mechanical properties of brain tissue in-vivo: experiment and computer simulation. *J Biomech*, 33(11):1369–1376, Nov 2000.

[43] A. Nabavi, P. M. Black, D. T. Gering, C. F. Westin, V. Mehta, R. S. Pergolizzi, M. Ferrant, S. K. Warfield, N. Hata, R. B. Schwartz, W. M. Wells III, R. Kikinis, and F. A. Jolesz. Serial Intraoperative MR Imaging of Brain Shift. *Neurosurgery*, 48:787–798, April 2001.

[44] G. M. Nielson and J. Sung. Interval Volume Tetrahedrization. In *Visualization '97*, pages 221–228. IEEE, 1997.

[45] S. Owen. A survey of unstructured mesh generation technology. Technical report, Department of Civil and Environmental Engineering, Carnegie Mellon University, Pittsburgh, PA15213 - USA, 1998. http://www.andrew.cmu.edu/user/sowen/survey/index.html.

[46] X. Papademetris, A. J. Sinusas, D. P. Dione, and J. S. Duncan. 3D Cardiac Deformation from Ultrasound Images. In *MICCAI 99: Second International Conference on Medical Image Computing and Computer-Assisted Intervention; October 1999; Cambridge, England.*, pages 420–429. Springer, September 1999.

[47] J. Park, D. Metaxas, and L. Axel. Analysis of Left Ventricular Wall Motion Based on Volumetric Deformable Models and MRI-SPAMM. *Medical Image Analysis*, 1(1):53–71, 1996.

[48] V. N. Parthasarathy, C. M. Graichen, and A. F. Hathaway. A Comparison of Tetrahedron Quality Measures. *Finite Element Analysis and Design*, 15:255–261, 1993.

[49] K. D. Paulsen, M. I. Miga, F. E. Kennedy, P. J. Hoopes, A. Hartov, and

D. W. Roberts. A Computational Model for Tracking Subsurface Tissue Deformation During Stereotactic Neurosurgery. *IEEE Trans. Biomed. Eng.*, 46(2):213–225, February 1999.

[50] W. Peckar, C. Schnörr, K. Rohr, and H. Stiehl. Parameter-Free Elastic Deformation Approach for 2-D and 3-D Registration Using Prescribed Displacements. *J. Math. Imag. Vision*, 10:143–162, 1999.

[51] O. Skrinjar, D. Spenser, and J. S. Duncan. Brain Shift Modeling for use in Neurosurgery. In *MICCAI 98: First International Conference on Medical Image Computing and Computer-Assisted Intervention; 1998 Oct 11–13; Boston, USA.*, pages 641–649. Springer-Verlag, 1998.

[52] O. Skrinjar, C. Studholme, A. Nabavi, and J. S. Duncan. Steps Toward a Stereo-Camera-Guided Biomechanical Model for Brain Shift Compensation. In *Information Processing in Medical Imaging (IPMI 2001), Davis, CA, USA, June 2001*, pages 183–189, 2001.

[53] O. M. Skrinjar and J. S. Duncan. Real Time 3D Brain Shift Compensation. In A. T.-P. A. Kuba, M. Smal, editor, *IPMI '99 : 16th International Conference on Information Processing in Medical Imaging*, volume 1613, pages 42–55. Springer, 1999.

[54] O. G. Staadt and M. H. Gross. Progressive Tetrahedralizations. In *Visualization '98*, pages 397–403. IEEE, 1998.

[55] J.-P. Thiran, V. Warscotte, and B. Macq. A Queue-based Region Growing Algorithm for Accurate Segmentation of Multi-Dimensional Images. *Signal Processing*, 60:1–10, 1997.

[56] P. Thompson and A. W. Toga. A Surface-Based Technique for Warping Three-Dimensional Images of the Brain. *IEEE Trans. Med. Imag.*, 15(4):402–417, 1996.

[57] T. C. T. Ting. *Anisotropic Elasticity: Theory and Applications*. Oxford University Press, 1996.

[58] E. K. Walsh and A. Schettini. Brain Tissue Elasticity and CSF Elastance. *Neurolog. Research*, 12:123–127, June 1990.

[59] S. K. Warfield, M. Ferrant, X. Gallez, A. Nabavi, F. A. Jolesz, and R. Kikinis. Real-Time Biomechanical Simulation of Volumetric Brain Deformation for Image Guided Neurosurgery. In *SC 2000: High Performance Networking and Computing Conference; 2000 Nov 4–10; Dallas, USA*, pages 230:1–16, 2000.

[60] W. M. Wells III, P. Viola, H. Atsumi, S. Nakajima, and R. Kikinis. Multimodal Volume Registration by Maximization of Mutual Information. *Med. Image Anal.*, 1:35–51, March 1996.

[61] C. Xu and J. L. Prince. Snakes, Shapes, and Gradient Vector Flow. *IEEE Trans. Image Processing*, 7(3):359–369, March 1998.

[62] O. C. Zienkewickz and R. L. Taylor. *The Finite Element Method*. McGraw Hill Book Co., New York, 4th edition, 1987.

Matthieu Ferrant was born in Islington (United Kingdom) in 1974. He received the Ph.D. and M.Sc. degrees in Electrical Engineering from the Université catholique de Louvain (Belgium) in april 2001 and june 1997 respectively. He has been a visiting student at the Institute for Perception Research (IPO) at the Eindhoven University of Technology (The Netherlands) within the Erasmus exchange program from february untill may 1997. From september '98 until june '99, he has been a visiting student at the Massachusetts Institute of Technology with Prof. Forbes Dewey within the International Consortium for Medical Imaging Technology. During that period, he also started working very closely with the Surgical Planning Laboratory at the Brigham and Woman's Hospital (Harvard Medical School, Boston MA) on medical applications with Simon Warfield. His main research interests concern deformable surface matching, rigid and non-rigid registration, finite element modeling, and multi-resolution surface representations.

Arya Nabavi was born in Teheran (Iran) in 1966. He received his MD. at the Christian Albrechts University Kiel (Germany) in 1991. In 2001 he became a Board certified Neurosurgeon. From April 1998 through April 2000 he worked at the Departments of Neurosurgery (PM.Black) and Radiology (F.A. Jolesz, R. Kikinis) at the Brigham and Womens Hospital (Harvard Medical School) in Boston, MA. supported by grants from the German Research Council (DFG) and the "Harvard Center of minimally invasive Surgery" (1998-1999 and 1999-2000 respectively). His work covers the fields of Computer assisted surgical applications and MR-guided Neurosurgery with special emphasis on the analysis and simulation of intraoperative deformations during brain surgery.

Benoît Macq was born in 1961. He received the Electrical Engineering and the PhD degrees from the Université catholique de Louvain (UCL, Belgium) in 1984 and 1989 respectively. He is currently Professor at the same university in the Telecommunications Laboratory since 1996. From 1992 to 1996 he was a senior researcher of the Belgian NSF at UCL, and invited assistant professor in the Telecommunications Laboratory. In 1990 and 1991, he worked on network planning for Tractebel S.A. in Brussels. He did his PhD thesis on perceptual coding for digital TV under the supervision of Prof. Paul Delogne at UCL. He has been visiting scientist at Ecole Polytechnique Fédérale de Lausanne (Switzerland) in 1995 and at the Massachusetts Institute of Technology (Cambridge, MA, USA) during the summer of 1999. He has been Visiting Professor at the Ecole Nationale Supérieure des Télécommunications, ENST-Paris and at the Université de Nice, Sophia-Antipolis, France from 1999 until 2000. His main research interests are image compression, image watermarking and image analysis for medical and immersive communications. He served as a Guest Editor for the Proceedings of the IEEE as well as for the Signal Processing Journal and is member of the program committee of several IEEE and SPIE conferences. He is Senior Member of the IEEE.

Ferenc A. Jolesz was born in Budapest, Hungary and received his M.D., and performed his residency in Neurosurgery there before moving to the United States in 1979. In Boston, he completed research fellowships in Neurology at Massachusetts General Hospital and in Physiology at Harvard Medical School, and a clinical residency and fellowship in Radiology at Brigham & Women's Hospital where he joined the staff as a neuroradiologist. A Professor of Radiology at Harvard Medical School, he has been Director of the Division of Magnetic Resonance Imaging at Brigham & Women's Hospital and more recently the Director of the Image Guided Therapy Program. His main research activities are in the areas of neuroradiology, neurophysiology, and developing new approaches to magnetic resonance imaging. Special interests include image guided therapy, interventional MRI and he is involved in investigations of various diseases of the central nervous system: demyelination, multiple sclerosis, schizophrenia and Alzheimer's disease. His research support has come from a variety of public and private sources, and he is currently the Principal Investigator of several NIH research grants, corporate-sponsored clinical trials, and industry supported research efforts. Dr. Jolesz has been elected member of the Institute of Medicine of the National Academy of Sciences and belongs to several professional societies and editorial boards of peer reviewed journals.

Ron Kikinis received his MD from the University of Zurich, Switzerland, in 1982. He has worked as a researcher at the ETH in Zurich and as a resident at the University Hospital in Zurich. He is currently the director of the Surgical Planning Laboratory of the Department of Radiology, Brigham and Woman's Hospital and Harvard Medical School, as well as an Adjoint Professor of biomedical engineering at Boston University. His research interests include the development of clinical applications for image processing, computer vision and interactive rendering methods. He is currently concentrating on developing fully automated segmentation methods and introducing computer graphics into the operating room.

Simon K. Warfield Dr. Warfield joined Brigham and Women's Hospital and Harvard Medical School in 1996. He was awarded a PhD in Computer Science and Engineering from the University of New South Wales, Sydney, Australia in 1997. His research in the field of medical image analysis is carried out in the Surgical Planning Laboratory of the Department of Radiology at Brigham and Women's Hospital, Boston. His research interests focus on methods for quantitative image analysis through novel segmentation and registration approaches, and in real-time image analysis, enabled by high performance computing technology, in support of surgery.